

# Global spherical harmonic models of the internal magnetic field of the Moon based on sequential and coestimation approaches

Michael E. Purucker<sup>1</sup> and Joseph B. Nicholas<sup>1</sup>

**Abstract.** Three new models of the global internal magnetic field of the Moon based on Lunar Prospector (LP) fluxgate magnetometer observations are developed for use in understanding the origin of the Moon's crustal magnetic field, and for modeling its interaction with the solar wind. The models are at spherical harmonic degree 170, corresponding to 64 km wavelength resolution, from 30 km mean altitude LP observations. Coverage is complete except for a few areas near each pole. Original signal amplitudes are best preserved in the sequential approach map, whereas feature recognition is superior in the coestimation and harmonic wavenumber correlation maps. Spherical harmonic degrees less than 15, corresponding to 666 km wavelength, are largely absent from the Moon's internal magnetic field. We interpret this bound in terms of the Moon's impact history. A derived magnetization map suggest magnetizations may locally exceed 0.2 A/m in the lunar crust at the survey resolution, if the crust is as thick as 40 km.

## 1. Introduction

Maps of the internal magnetic field of the Moon find use in deciphering the early history of the Moon, especially whether it possessed a primordial dynamo field [Fuller, 1998; Garrick-Bethell *et al.*, 2009]. More generally, we are interested in how these internal fields originate, because the Moon does not possess a dynamo-driven field at present. If it did, then rocks which cooled below their Curie temperature would acquire a thermal remnant magnetization (TRM), just as in the terrestrial case. The other leading candidate for the origin of these internal fields is via the amplification of existing fields during large basin-forming impacts [Hood and Artemieva, 2008].

Internal magnetic fields at the Moon were first recognized by particles and fields instruments onboard the Apollo 15 and 16 subsatellites. The polar-orbiting Lunar Prospector [Binder, 1998] provided the first global mapping of the lunar magnetic field from low (11-66 km) orbit in 1998 and 1999. Both electron reflectometer [Halekas *et al.*, 2001] and triaxial fluxgate magnetometers [Hood *et al.*, 2001] provided mappings. The electron reflectometer employs a remote sensing approach to place bounds on the magnitude of the magnetic field at the surface, while the magnetometer measures the direction and strength of the vector magnetic field at the satellite. Lunar Prospector was followed in 2007 and 2008 by the Japanese Kaguya satellite, which mapped the magnetic fields at an altitude of 100 km utilizing a triaxial fluxgate magnetometer [Matsushima *et al.*, in press; Toyoshima *et al.*, 2008; Shimizu *et al.*, 2008; Takahashi *et al.*, 2009].

Previous maps of the magnetic field, based on the missions above, include local, space domain maps [Tsunakawa *et al.*, in press] and global, spherical harmonic [Purucker, 2008] maps to spherical harmonic degree 150. Maps based on the magnetometer data include those of [Richmond and Hood, 2008], while those based on the electron reflectometer data include those of [Mitchell *et al.*, 2008].

## 2. Data

The low-noise (6 pT RMS) fluxgate magnetometers on the spin-stabilized Lunar Prospector spacecraft were mounted on a 2.5 m boom in order to minimize spacecraft influences. The spin-averaged measurements of the nominal 18 Hz magnetic field observations are at 5 second intervals, corresponding to an along-track sampling of 9 km. Our analysis first converted the Level 1B data from NASA's Planetary Data System (PDS, UCLA, Particles and Fields node) to a local tangent coordinate system with  $B_r$  positive outward,  $B_\theta$  positive southward, and  $B_\phi$  positive eastward.

Three lunar magnetic regimes are distinguished. The wake regime represents observations made in the lunar wake, when the Sun is obscured by the Moon. The solar wind regime represents observations made when the Sun is visible from the satellite, and out of the Earth's magnetotail. The tail regime represents observations made within the Earth's magnetotail. A fourth regime represents observations made within the Earth's magnetosheath. This regime is transitional between the tail and wind regimes, and data sampled there are not included in the final maps made using our procedures. All maps shown here utilize data collected only in the wake and tail regimes. It has been previously shown [Purucker, 2008] that maps made using data from solar wind times are compressed and distorted relative to those from wake and tail times.

## 3. Model development and parameterization

Two different parameterizations are used to characterize the internal magnetic field of the Moon. We do this because different parameterizations allow us to emphasize different attributes of the solution, and to determine error limits on the solutions. We first describe our overall philosophy of model development. We then briefly describe the sequential approach, using a line of dipoles to characterize the internal field along a spacecraft track [Purucker, 2008]. We next describe, in detail, a coestimation approach, using a harmonic basis to characterize the internal field. We finish up this section by describing the strengths and limitations of these two approaches.

Our philosophy is dictated by the computational problems associated with developing least squares models of large data sets. Even in conjugate gradient approaches [Purucker *et al.*, 1996], the memory requirements go as  $O(po)$  where

<sup>1</sup>Raytheon at Planetary Geodynamics Laboratory, Code 698, Goddard Space Flight Center, Greenbelt, MD 20771

$p$  is the number of parameters and  $o$  the number of observations. The least-squares models described here have in excess of 32000 parameters, and 2.7 million observations. Instead of trying to develop this large model in 2-dimensions, we develop them in 1-dimension using the along-track and radial components of three adjacent passes collected during a particular lunar regime. As long as the distance between adjacent passes is less than or similar to the distance above the magnetic source, the adjacent passes will be sensitive to common internal magnetic sources. We then extend our models from 1- to 2- dimensions using the Driscoll and Healy sampling theorem [Driscoll and Healy, 1994].

### 3.1. Line dipole approach

The external magnetic field in the sequential, line dipole approach is represented as a uniform field over each satellite half orbit, and the half-orbits extend from pole to pole. The technique was first described by Nicholas *et al.* [2007] and later by Purucker [2008]. The external field was determined in a least-squares sense from all three components of the vector data. Following the removal of the external field model from each half-orbit, an internal line dipole model is developed in spherical coordinates [Dyment and Arkani-Hamed, 1998], utilizing three adjacent half-orbits which are separated in space by about one degree (30 km), and in time by 1.9 hours. The crust under the three adjacent half-orbits is divided into blocks, each of which is assumed to have a magnetic dipole at its center. A horizontal dipole is located under each observation of the center pass, on the 1737.1 km mean lunar radius surface.

The magnetic field is represented as the gradient of a scalar magnetic potential

$$V(r, \theta, \phi) = -\vec{M} \cdot \nabla \left( \frac{1}{l} \right) \quad (1)$$

where  $\vec{M}$  is the dipole moment and

$$l = \sqrt{r^2 + r'^2 - 2rr' \cos \zeta} \quad (2)$$

where  $l$  is the distance between the source and the dipole and  $\zeta$  is the angle between  $r$  and  $r'$ .

$\vec{M}$  is constrained by observations of  $B_r$  and  $B_\theta$ , and in the previous implementation of this approach for the Moon [Purucker, 2008] the distance between the source and the dipole for the observations of  $B_\theta$  was incorrect by a factor of  $l$ . This had the effect of decreasing the amplitude of the resulting map of  $B_r$ , but did not change the location of the magnetic features, as we will show. As before, we utilized a preconditioned conjugate gradient approach [Purucker *et al.*, 1996], and iterated each solution six times. Each solution, of which there were in excess of 5000 low-altitude ones, was used to calculate the radial magnetic field at an altitude of 30 km above the mean lunar radius. Figure 2 shows the radial magnetic field profiles and grids over the Reiner Gamma swirl [Nicholas *et al.*, 2007], one of the largest isolated magnetic features on the Moon. Figure 3 shows the radial magnetic profiles and grids over the northwestern corner of the South Polar Aitken basin, the location of the most extensive set of magnetic features on the Moon. Profiles and maps before and after the major processing steps are shown, and emphasize the clarification of the features which occurs after each processing step. As can be seen, individual magnetic features are located in the same position in the two approaches, and the major difference seen here is in the difference in the magnitude of the magnetic features. This will be discussed further below.

### 3.2. Harmonic approach

The second parameterization utilizes a harmonic approach to characterize the internal magnetic field, and co-

estimates the internal and external magnetic fields. The external magnetic fields are still described, as in the sequential approach, as a uniform external field over each satellite half-orbit.

We again utilize both  $B_r$  and  $B_\theta$  observations to constrain the model, and represent those vectors as the gradient of a scalar magnetic potential

$$B_r = -\frac{\partial V}{\partial r} = \sum_{n=1}^{180} \left[ (n+1)g_n^0 \left( \frac{a}{r} \right)^{n+2} \right] P_n^0(\theta) \quad (3)$$

$$B_\theta = -\frac{1}{r} \frac{\partial V}{\partial \theta} = -\sum_{n=1}^{180} \left[ g_n^0 \left( \frac{a}{r} \right)^{n+2} \right] \frac{dP_n^0(\theta)}{d\theta} \quad (4)$$

where  $a$  is the mean radius of the Moon,  $P_n^0$  are the associated Legendre functions of degree  $n$  and order 0, and the  $g_n^0$  are the internal coefficients to be determined from observations of  $B_r$  and  $B_\theta$  at radial distance  $r$  from the center of the Moon [Langel, 1987]. The resulting fields calculated from the model are continued to an altitude of 30 km. The

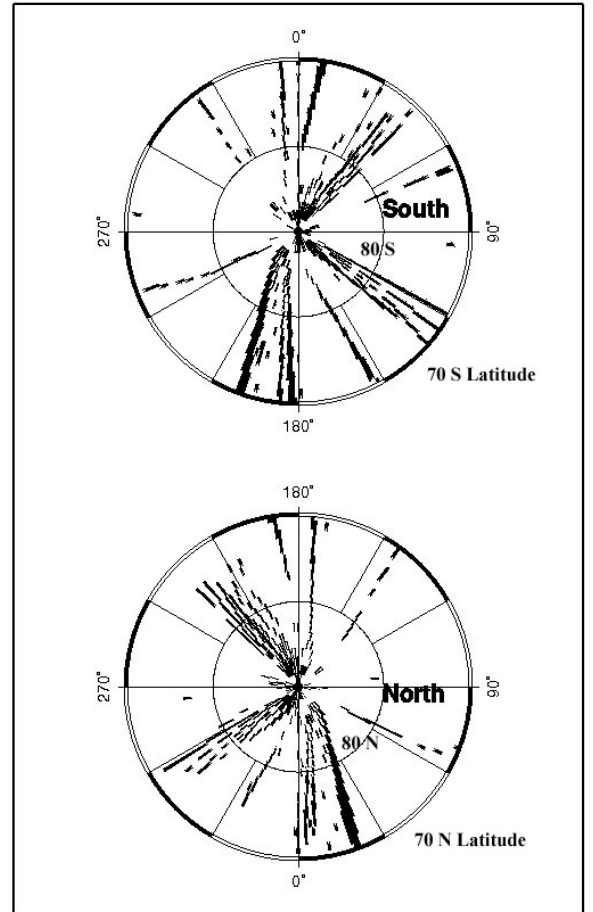


**Figure 1.** The location of bins in the polar regions (within 20 degrees of the poles) for which we have no observations.

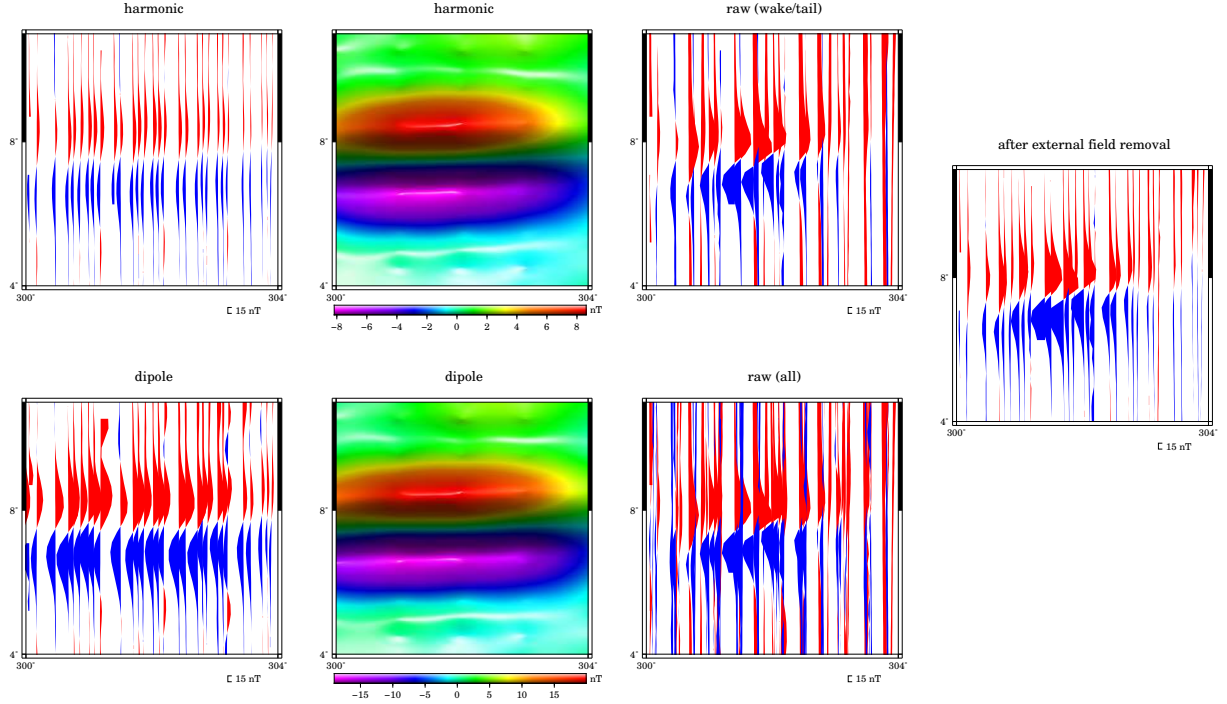


**Figure 2.** Radial magnetic field from sequential and coestimation approaches over Reiner Gamma, showing individual profiles and map views. The individual profiles are colored red where they are positive, blue where they are negative. The profile labeled ‘raw(all)’ includes data from all lunar regimes and represents the starting point of both the sequential and coestimation approaches. The subset of raw data from wake and tail times is shown immediately above that. The sequential approach first removes a uniform external field from the observations, and the resulting radial fields from wake and tail times are shown on the far right. On the left are shown final profiles and grids after completion of the sequential dipole and harmonic coestimation approaches. Cylindrical equidistant projection.

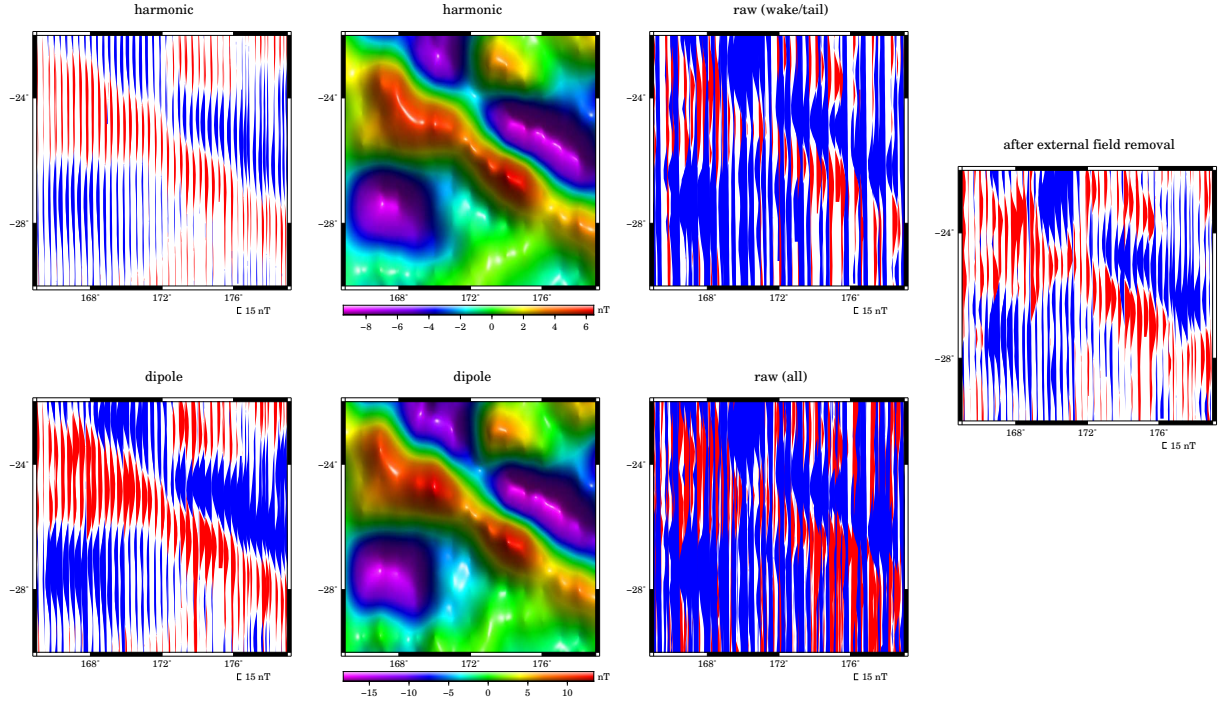


**Figure 3.** Radial magnetic field from sequential and coestimation approaches over the South Polar-Aitken basin region showing individual profiles and map views. See Figure 2 for further details.

least squares problem is solved using singular value decom-

position. In a variant of this approach, we first demean the individual profiles because of the absence of a monopole term

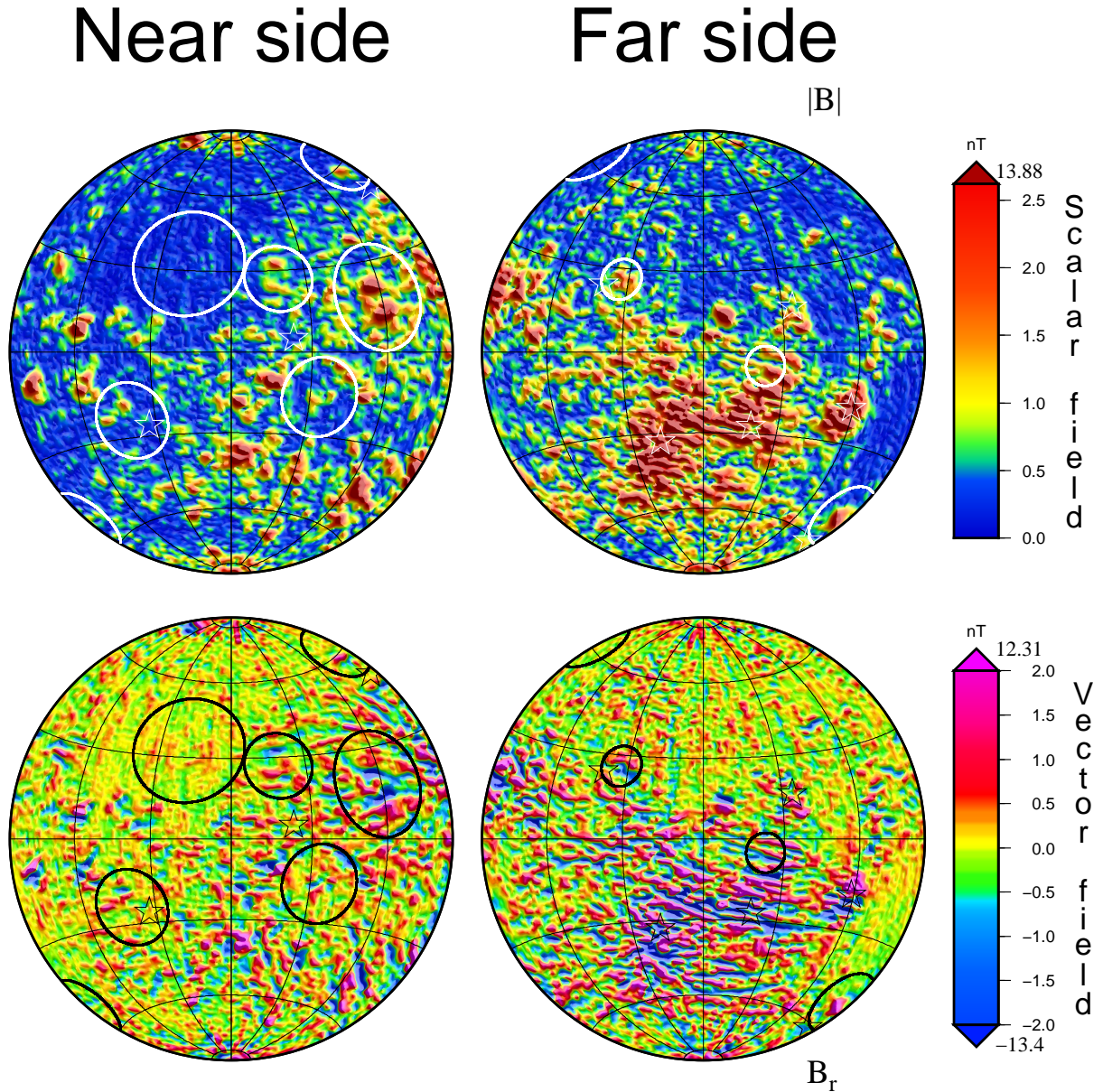


**Figure 4.** Map made using coestimation (harmonic for internal and uniform field for external) approach. See Figure 5 for further details. Antipodes of the basins are shown as unnumbered stars.

in our solution. We find that this variant approach yields solutions that are almost indistinguishable, in terms of the magnitude and location of the resulting magnetic features, to our standard approach.

### 3.3. Strengths and limitations

Coestimating the internal and external magnetic fields allows for an estimate of the covariance of the solution, in contrast to the sequential approach where no such information is available. This information allows us to conclude that the internal magnetic field is correlated most strongly with the external field at degree 2. Lesser correlations are seen at degrees 4, 6, 1, and 3. As a consequence, we have removed internal degrees 1 through 3 from the final 1-D solutions.

The coestimation approach assumes that the longitude of the three adjacent passes are identical. This limitation of the coestimation approach has the effect of suppressing significantly the amplitude of the anomalies, as can be seen in Figure 2 and Figure 3. This suppression seems to be largest

in magnetic features which have E-W extents comparable to the width of the three adjacent passes, or approximately two degrees. Reiner Gamma (Figure 2) is an example of such a feature, and we see larger amplitude suppressions here than in the South Polar Aitken region (Figure 3).

Both approaches share some additional limitations. They are not able to incorporate the  $B_\phi$  component into the modeling because  $B_\phi$  is sensitive to the E-W extent of a magnetic source. However,  $B_\phi$  is usually the component most affected by poorly modeled external and toroidal fields, and so neglecting it is justified on other grounds. A more important limitation is that internal magnetic fields parallel to the polar-orbiting LP spacecraft are not as well-characterized as those in other directions.

## 4. From 1-D to 2-D

The radial magnetic field model data sets resulting from the sequential and coestimation approaches just described are binned into 360 by 360 equiangular bins, one degree



in longitude by one-half degree in latitude. Median fields for wake and tail times are then calculated for each bin in order to produce a robust estimate of the field, minimally affected by outliers. More than 99% of the bins were populated for each of the approaches. The unpopulated bins are concentrated in a few areas within 20 degrees of the poles, as shown in Figure 1. The binned data is then fit to a continuous curvature surface [Wessel and Smith, 1998] with adjustable tension set to 0.25, appropriate for potential field observations.

## 5. Spherical harmonic models of magnetic field and magnetization

The gridded data sets representing the sequential and coestimation approaches are then utilized to construct spherical harmonic models to degree and order 180 with the Driscoll and Healy sampling theorem [Driscoll and Healy, 1994], and shown in Figure 5 and Figure 4, respectively.

The magnetic potential is traditionally represented as

$$V = a \sum_{n=1}^{180} \left(\frac{a}{r}\right)^{n+1} \sum_{m=0}^n [g_n^m \cos(m\phi) + h_n^m \sin(m\phi)] P_n^m(\theta) \quad (5)$$

where  $\theta$  is colatitude, and  $\phi$  longitude,  $P_n^m$  are the Schmidt quasi-normalized associated Legendre functions of degree  $n$

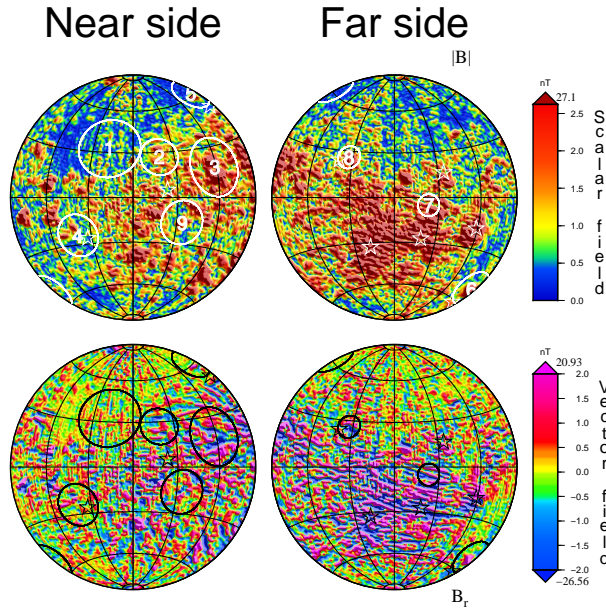


**Figure 5.** Global spherical harmonic model of the lunar magnetic field at an altitude of 30 km above the mean lunar radius made using the sequential (dipole) approach. From top to bottom: Scalar magnitude and radial component fields. Near side maps are shown on the left, far side on the right. Illumination is from the north or east. Lambert equal area projection. Large impacts are shown as white circles and are numbered to correspond with their names: 1) Imbrium, 2) Serenitatis, 3) Crisium, 4) Humorum, 5) Humboldtianum, 6) Mendel-Rydberg, 7) Korolev, 8) Moscoviense, and 9) Nectaris. The maximum and minimum values over the entire map are shown above and below the colored triangles which define the end points of the scale.

and order  $m$ , and the  $g_n^m$  and  $h_n^m$  are the coefficients of the model.

An assessment of the correlation of the two maps can be made in the spherical harmonic domain using degree correlations [Langel and Hinze, 1998], defined as

$$\rho_n = \frac{\sum_{m=0}^n (g_{nm} g'_{nm} + h_{nm} h'_{nm})}{\sqrt{[\sum_{m=0}^n (g_{nm}^2 + h_{nm}^2)] [\sum_{m=0}^n (g'_{nm}^2 + h'_{nm}^2)]}} \quad (6)$$

for each degree  $n$ .

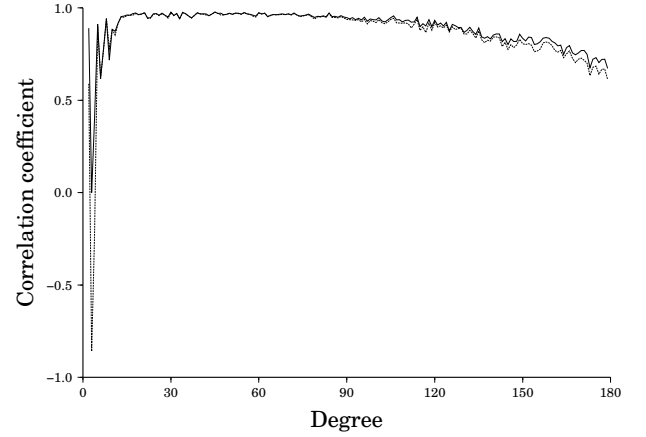


**Figure 6.** Correlation, by spherical harmonic degree, of the sequential and coestimation approaches. Dotted lines show the correlation before application of the harmonic wavenumber correlation technique, solid lines are after application of the technique.

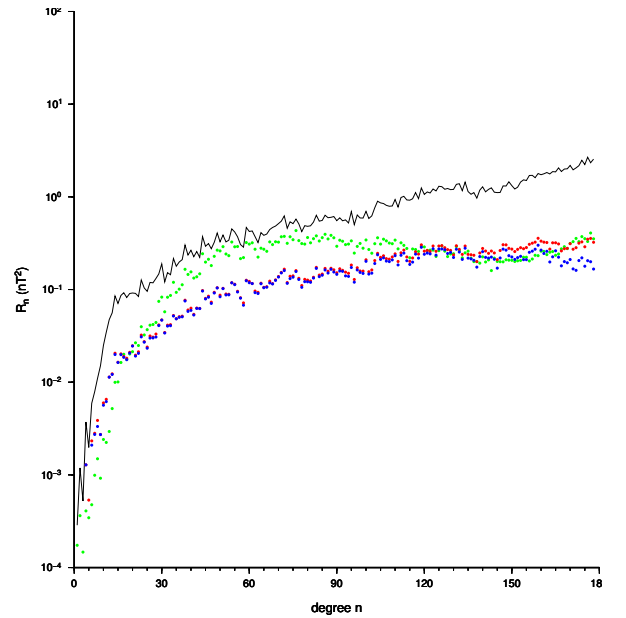


**Figure 7.** Lowes-Mauersberger [Lowes, 1974] power spectra of sequential (solid black line), coestimation (red dots), and correlative (blue dots) approaches, and previous sequential approach (green dots) [Purucker, 2008].  $R_n$  is the mean square amplitude of the magnetic field produced by harmonics of degree  $n$ .

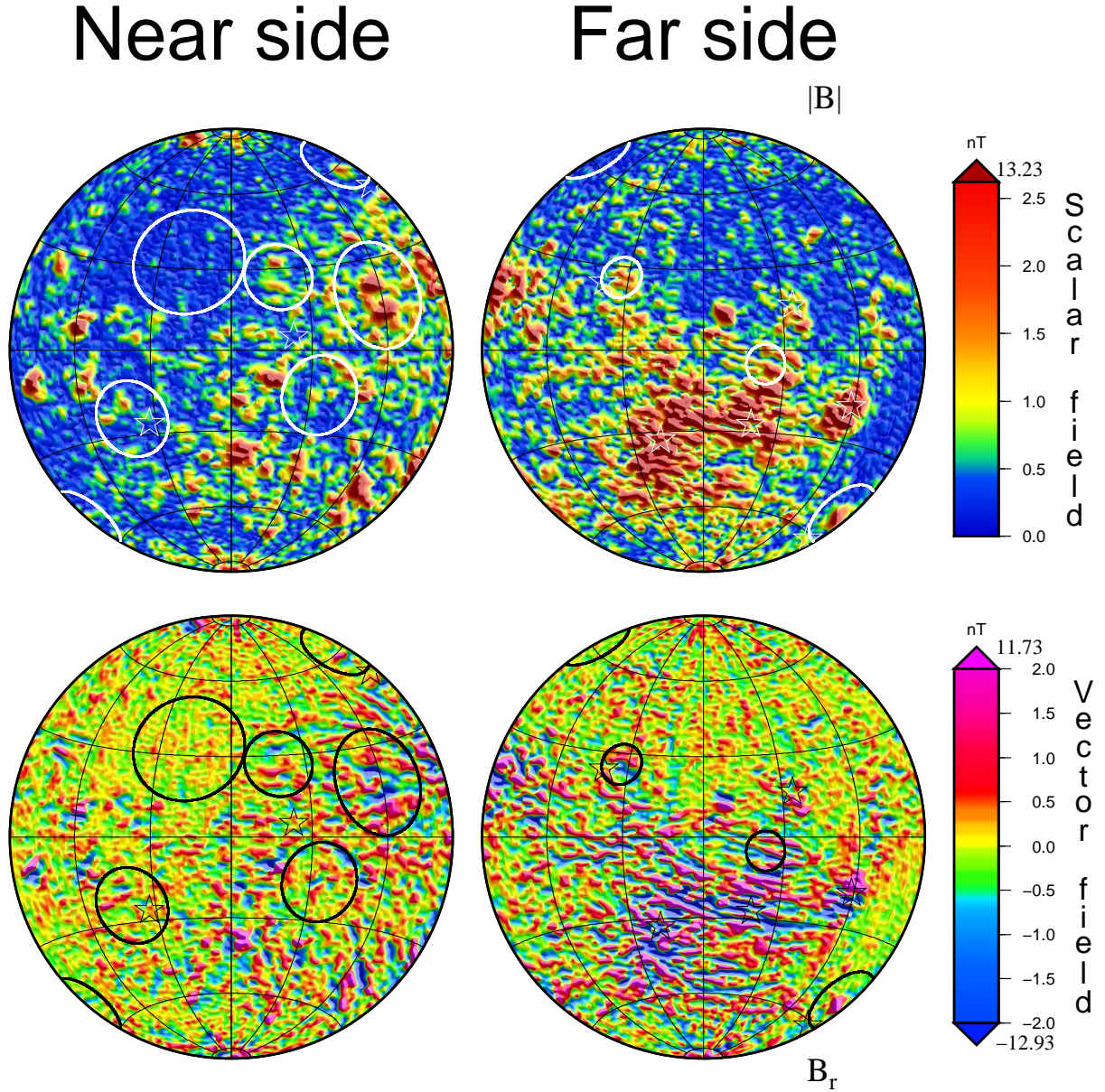


**Figure 8.** Combined radial and scalar magnetic field from sequential and coestimation approaches, retaining degrees with phases separated by less than 30 degrees. Spherical Harmonic degrees 1 through 170. Antipodes of the basins are shown as unnumbered stars. See Figure 5 for further details.

The degree by degree correlations of these two maps (Figure 6) indicate high correlations between degrees 15 and 170, decreasing slightly at the highest degrees. We present all of our maps between degrees 1 and 170 because degree correlations between our two maps dip below 0.75 at about degree 170. The low correlations between degrees 1 and 14 suggest that users might also wish to omit, or interpret with care, information from those lowest degrees. All of our model coefficients, maps and codes, are available on our web site at <http://core2.gsfc.nasa.gov/research/purucker/moon2010>.

We apply a harmonic wavenumber correlation technique [Langel and Hinze, 1998] to extract common features of the two maps (Figure 8), retaining coefficients from the coestimation map that differ by less than 30% phase angle from their counterparts in the sequential map. This technique is often applied in geomagnetic applications [Langel and Hinze, 1998] in order to minimize the influence of non-crustal components in the final map. While emphasizing the common features, it also sometimes reduces the amplitude of the map

significantly. In this case, only minimal amplitude reduction was noted from the coestimation map. The choice of phase angle, or equivalently, correlation, is a subjective one but the trade to be assessed is between removing non-correlative magnetic field components on one hand, and amplitude reduction on the other hand. The phase angle selected, 30%, does a good job of removing non-correlative components while minimizing amplitude reduction.

The phase angle of each degree and order is defined as

$$\zeta_{nm} = \tan^{-1} \left( -\frac{h_{nm}}{g_{nm}} \right) \quad (7)$$

The phase angle difference is related to the correlation between the components as follows.

$$\rho_{nm} = \cos(\zeta_{nm} - \zeta'_{nm}) \quad (8)$$



The Lowes-Mauersberger [Lowes, 1974] power spectra is often used to characterize large scale features of the solution. It is defined as the mean square amplitude of the magnetic field produced by harmonics of degree  $n$ , or formally,

$$R_n = (n+1) \sum_{m=0}^n [(g_n^m)^2 + (h_n^m)^2] \quad (9)$$

The power spectra of the sequential and coestimation approaches (Figure 7) exhibit a significant difference in amplitude, ascribable to the regularization inherent in the coestimation approach. The two approaches exhibit very similar shapes, in contrast to the shape of the power spectrum of Purucker [2008].

The difference between the shapes of the spectra is ascribable to the incorrect incorporation of the  $B_\theta$  field into the Purucker [2008] model, described earlier, a deficiency that does not affect the location of the magnetic features, only their strength, as can be seen by comparing local features, such as in and around the Serenitatis impact basin (Figure 9).

The lack of power at degrees 1-14 in all of the maps, and the low correlations between the sequential and coestimation

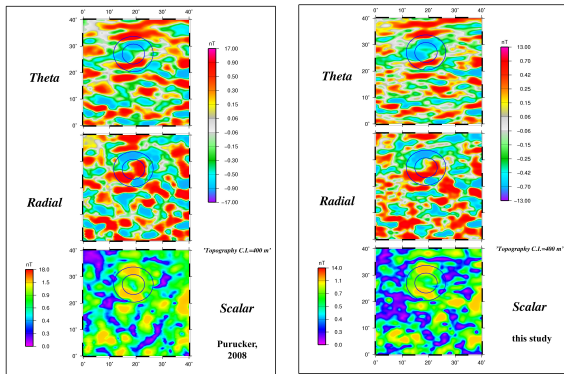


**Figure 9.** Magnitude, radial, and theta fields over the Serenitatis impact crater (inner and outer ring shown) in this study (harmonic correlation map) compared with the map of Purucker (2008). Azimuthal equidistant projection.

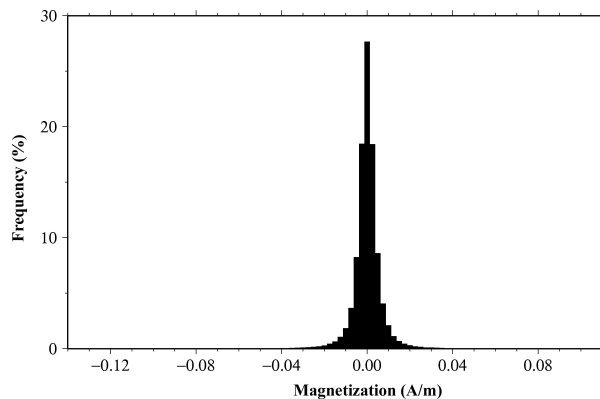


**Figure 10.** Histogram showing the distribution of magnetizations (range is  $-0.14$  A/m to  $0.10$  A/m) calculated from the sequential model, made using a space domain, conjugate gradient approach [Purucker *et al.*, 1996]. Magnetization values assume a 40 km thick crust.

approaches, suggest a critical change in lunar properties at about this degree. Degree 15 corresponds to a wavelength of 666 km on the Moon, and the power spectra suggest that there are no magnetic features with wavelengths longer than this on the Moon. Many of the Nectarian-aged craters, such as Serenitatis (Figure 9) have magnetic features associated with them, and many of the larger Nectarian craters are in the 600 km size range.

A magnetization map of the resulting field is made assuming radially oriented magnetization directions, and as a consequence it looks similar to the  $B_r$  map (Figure 8). The magnetization map suggests magnetizations may locally exceed 0.1 to 0.2 A/m (Figure 10) in the lunar crust at the resolution of the survey (64 km), if the crust is as thick as 40 km.

The ambiguities inherent in the magnetization inverse problem allow uniformly magnetized shells of any amplitude to be added to the magnetization solution, with no effect on the measured magnetic field outside of the shell [Runcorn, 1975]. This means that it is impossible to distinguish between some plausible geologic scenarios unless samples of the magnetized bodies are available. As an example, there are two plausible geologic scenarios which might be appropriate for the Moon in the South Polar Aitken region (Figure 3). The first interpretation posits oppositely magnetized bodies implaced adjacent to one another, and the second interpretation posits similarly magnetized bodies implaced at some larger distance apart, and with larger magnetizations. Similar ambiguities have been noted in the linear, strongly magnetic features of the Terra Sirenum region of Mars [Acuña, personal communication].

## 6. Discussion

Comparison of the new magnetic field maps with the electron reflectometer map (Figure 11) of Mitchell *et al.* [2008] reveal little difference from previous assessments [Purucker, 2008]. The magnetic map made using the harmonic wavenumber correlation approach correlates with the electron reflectometer map with a linear correlation coefficient [Press *et al.*, 1992] of 0.60.

As expected, the magnetic map also correlates strongly with the preliminary magnetic map of Purucker [2008] with

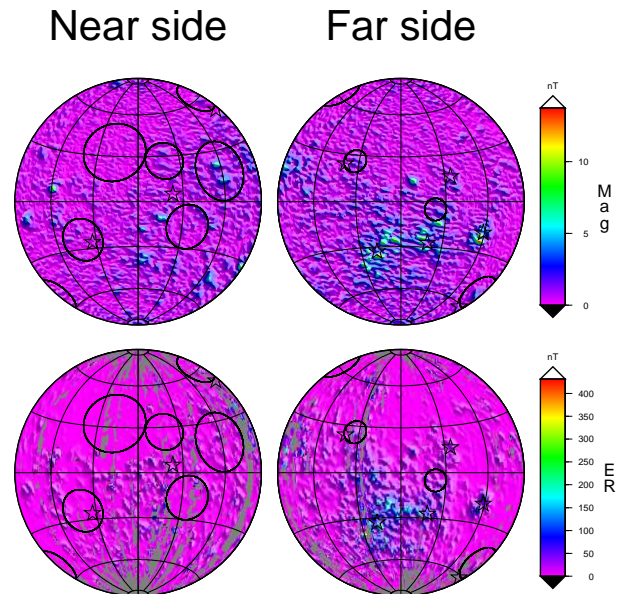


**Figure 11.** Magnitude of magnetic field measured by the Magnetometer (MAG) and Electron Reflectometer (ER) instruments onboard Lunar Prospector. See Figure 5 for further details.

a linear correlation coefficient of 0.9. The new magnetic map also correlates well with the new Kaguya magnetic map (Figure 12) of *Tsunakawa et al.* [in press]. Both utilized vector fluxgate magnetometers as the source of their observations. However the Kaguya spacecraft was at much higher altitudes (100 km vs 30 km), and was a three-axis stabilized spacecraft in contrast to Lunar Prospector, which was spin-stabilized. A map of the radial magnetic fields at 30 km and 100 km reveal the presence of the WNW-trending patterns over the South Polar Aitken basin region in both maps, although the pattern is considerably attenuated in the Kaguya map, because of its 100 km altitude. Upward comparison of our sequential and coestimation maps to 100 km altitude reveal virtually identical features in the Kaguya and Lunar Prospector maps (Figure 12). We also note that the amplitude of our upward continued coestimation map agrees most closely with the Kaguya map. The amplitudes from our sequential map are slightly higher than those seen in the Kaguya map. Detailed comparison awaits the release of the Kaguya model in digital form.

The error levels of the two maps can be assessed by means of maps of the rejected components of the harmonic wavenumber correlation approach (Figure 13). These maps reveal that the errors are scattered about the surface, and are small.

We expect that the maps will be utilized to further understanding of lunar tectonics (Figure 3), basins (Figure 9), swirls (Figure 2), and the nature of the primordial lunar field.

We expect that future maps made using Lunar Prospector data may be able to increase the map resolution, at least locally. The ultimate limit is set by the spin averaging (9 km along track) of the Lunar Prospector data, which yields 3 observations per degree latitude. This corresponds to 540 field samples from pole to pole, which would theoretically [Driscoll and Healy, 1994] allow a degree and order 270 model to be developed. However, only 96% of the 1/3rd by 2/3rd degree bins corresponding to a degree 270 model are filled, in contrast to more than 99% in the present model. However, there are still improvements to be made that would increase the fidelity of the maps. Future enhancements to internal lunar magnetic models certainly include more physically-based models of the external magnetic field and particles environment, and inclusion of information on anisotropic errors in the Lunar Prospector measurements. Lunar Prospector was spin-stabilized, and we expect that magnetic fields will be most accurately determined in the spin plane. Although this directional information is not included in the Level 1B data set, it might realistically be extracted from archived spacecraft data.

## 7. Conclusion

This study presents the highest resolution maps of the internal magnetic field of the Moon available to date. Magnetic fields with wavelengths in excess of 666 km are largely absent from the Moon, a consequence of its cratering history. Even higher resolution maps of the internal magnetic field would allow for a much expanded understanding of the processes at work in the lunar interior and surface. While surface measurements would provide the highest resolution, they would also be the most expensive to obtain, and global coverage would be prohibitively expensive. A possible approach to providing higher resolution would involve magnetic gradiometry from two or more satellites flying nearby, or in a string of pearls configuration. Such a configuration will be employed to map the Earth's crustal field by the upcoming Swarm satellites [Friis-Christensen et al., 2009].

The digital data, maps, and code presented in this manuscript can be obtained from <http://core2.gsfc.nasa.gov/research/purucker/moon2010>.

**Acknowledgments.** We would like to acknowledge the Lunar Prospector team and especially the late Mario Acuña for the collection of this dataset. M. Wieczorek, J. Head, N. Olsen, J. Halekas, D. Clark, V. Lesur, T. Sabaka, H. Tsunakawa, I. Garrick-Bethell, C. Russell, K. Whaler, and L. Hood provided valuable comments, data sets, or codes. We thank M. Mandea for providing an uninterrupted time for writing at Boiscommun, and B. Langlais, R. Lillis, D. Blewett, J. Slavin, and H. Frey for stimulating discussions on related topics. A. Isac provided assistance with the figures. Purucker and Nicholas were supported by a NASA Discovery Data Analysis Program (DDAP) contract. GMT [Wessel and Smith, 1998] was used for the graphics, and some analysis. SHTOOLS, by M. Wieczorek (IPGP), was used to implement the Driscoll and Healy sampling theorem [Driscoll and Healy, 1994].

## References

- Binder, A. (1998), Lunar Prospector Overview, *Science*, **281**, 1475–1476.
- Driscoll, J. R., and D. M. Healy (1994), Computing Fourier transforms and convolutions on the 2-sphere, *Adv. Appl. Math.*, **15**, 202–250.
- Dyment, J., and J. Arkani-Hamed (1998), Equivalent source dipoles revisited, *Geophys. Res. Lett.*, **25**, 2003–2006.
- Friis-Christensen, E., H. Lühr, G. Hulot, R. Haegmans, and M. Purucker (2009), Geomagnetic Research from Space, *EOS TRANSACTIONS AGU*, **90**(25), 213–214.
- Fuller, M. (1998), Lunar magnetism—a retrospective view of the Apollo sample magnetic studies, *Phys. Chem. Earth*, **23**, 725–735.
- Garrick-Bethell, I., B. Weiss, S. D.L., and J. Buz (2009), Early lunar magnetism, *Science*, **323**, 356–359.
- Halekas, J. S., D. L. Mitchell, R. P. Lin, S. Frey, M. H. Acuña, and A. B. Binder (2001), Mapping of lunar crustal magnetic fields using lunar prospector electron reflectometer data, *J. Geophys. Res.*, **106**, 27,841–27,852.
- Hood, L., and N. Artemieva (2008), Antipodal effects of lunar basin-forming impacts: Initial 3-d simulations and comparisons with observations, *Icarus*, **193**, 485–502.
- Hood, L. L., A. Zakharian, J. Halekas, D. L. Mitchell, R. P. Lin, M. H. Acuña, and A. B. Binder (2001), Initial mapping and interpretation of lunar crustal magnetic anomalies using Lunar Prospector magnetometer data, *J. Geophys. Res.*, **106**, 27,825–27,839.
- Langel, R. A. (1987), *Geomagnetism*, chap. The main geomagnetic field, Academic Press.
- Langel, R. A., and W. J. Hinze (1998), *The magnetic field of the Earth's lithosphere: The satellite perspective*, Cambridge University Press.
- Lowes, F. J. (1974), Spatial power spectrum of the main geomagnetic field, and extrapolation to the core., *Geophys. J. R. Astron. Soc.*, **36**, 717–730.
- Matsushima, M., et al. (in press), Magnetic cleanliness program under control of electromagnetic compatibility for the SELENE (Kaguya) spacecraft, *Space Science Reviews*.
- Mitchell, D., J. Halekas, R. Lin, S. Frey, L. Hood, M. Acuña, and A. B. Binder (2008), Global mapping of Lunar crustal magnetic fields by Lunar Prospector, *Icarus*, **194**, 401–409.
- Nicholas, J., M. Purucker, and T. Sabaka (2007), Age spot or youthful marking: Origin of Reiner Gamma, *Geophysical Research Letters*, **34**, doi:{10.1029/2006GL027794}.
- Press, W., S. Vetterling, and W. Flannery (1992), *The Art of Scientific Computing*, 2nd edition, Cambridge University Press.
- Purucker, M. (2008), A global model of the internal magnetic field of the moon based on lunar prospector magnetometer observations, *Icarus*, **197**, 19–23.
- Purucker, M., T. Sabaka, and R. Langel (1996), Conjugate gradient analysis: a new tool for studying satellite magnetic data sets, *Geophys. Res. Lett.*, **23**, 507–510.
- Richmond, N., and L. Hood (2008), A preliminary global map of the vector lunar crustal magnetic field based on Lunar Prospector magnetometer data, *Journal of Geophysical Research-Planets*, doi:{10.1029/2007JE002933}.



- Runcorn, S. (1975), On the interpretation of lunar magnetism, *Phys. Earth Plan. Int.*, 10, 327–335.
- Shimizu, H., F. Takahashi, N. Horii, A. Matsuoka, M. Matsushima, H. Shibuya, and H. Tsunakawa (2008), Ground calibration of the high-sensitivity SELENE lunar magnetometer LMAG, *Earth, Planets, and Space*, 60, 353–363.
- Takahashi, F., H. Shimizu, M. Matsushima, H. Shibuya, A. Matsuoka, S. Nakazawa, Y. Iijima, H. Otake, and H. Tsunakawa (2009), In-orbit calibration of the lunar magnetometer onboard SELENE (KAGUYA), *Earth, Planets, and Space*, 61, L1269+.
- Toyoshima, M., H. Shibuya, M. Matsushima, H. Shimizu, and H. Tsunakawa (2008), Equivalent source mapping of the lunar crustal magnetic field using ABIC, *Earth, Planets, and Space*, 60, 365–373.
- Tsunakawa, H., H. Shibuya, F. Takahashi, H. Shimizu, M. Matsushima, A. Matsuoka, S. Nakazawa, H. Otake, and Y. Iijima (in press), Lunar magnetic field observation and initial global mapping of lunar magnetic anomalies by MAP-LMAG on-board SELENE (kaguya), *Space Science Reviews*.
- Wessel, P., and W. Smith (1998), New improved version of Generic mapping tools released, *EOS Trans. AGU*, 79, 579.

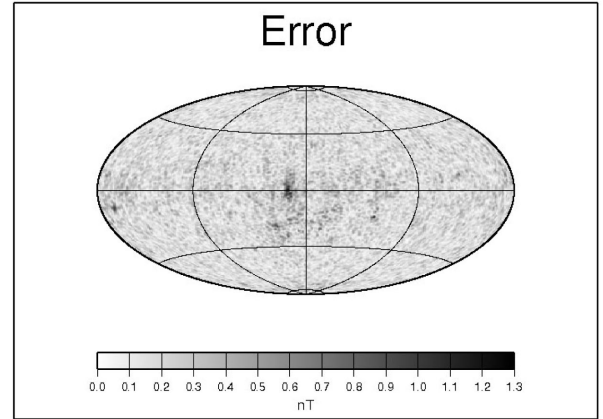


**Figure 13.** Magnitude of the rejected component of the harmonic map. Hammer projection extending from 0 to 360 Longitude.

